Engineering and Technology Journal
Journal homepage: https://etj.uotechnology.edu.iq

Mapping agricultural lands at risk of meteorological drought in iraq using geostatistics

Mohammed H. Azeez[a,b*], **Hisham M. Jawad Al Sharaa**[b], **Abdul Razzak T. Ziboon**[c]

[a] Surveying Dept., Shatra Technical Institute (STI), Southern Technical University (STU), Alshtra, Iraq.
[b] Civil Engineering Dept., University of Technology-Iraq, Alsina'a street, 10066 Baghdad, Iraq.
[c] College of Engineering, Al-Esraa University, Baghdad, Iraq.
*Corresponding author Email: mohammed.aziz@stu.edu.iq

HIGHLIGHTS

- Create a model to identify areas that use river irrigation and those that use seasonal irrigation.
- An overall methodology identified vulnerable agricultural areas at risk of meteorological drought in time and space.
- The BEAST model performed well in time series analysis, making the geostatistical model applicable to all land covers
- The geostatistical model is applicable globally at the pixel level for comprehensive analysis.

Keywords:
Drought
Vulnerability
Land degradation
Spatial modeling
Cropland

ABSTRACT

Identifying vulnerable agricultural lands at risk of meteorological drought is challenging for researchers. Its complexity lies in the fact that agricultural lands are irrigated by two sources: rain and rivers. In this research, we have developed a geostatistical model to separate river-dependent lands unaffected by meteorological drought waves and land vulnerable to the risk of meteorological drought. The inputs of this geostatistical model are the vegetation index and the humidity index extracted from Landsat 8, the rainfall from CHIRPS, and the LULC from ESA. The correlation between the Normalized Difference Vegetation Index (NDVI), the Normalized Difference Moisture Index (NDMI), and the rainfall was tested using the Pearson Correlation Coefficient (PCC) for more than five million pixels representing agricultural lands in Dhi-Qar Iraq. The Getis-Ord Gi* statistical index was used to cluster each pixel according to PCC value. This model achieved accurate results as it was validated using ground truth and the BEAST (Bayesian Estimator of Abrupt Change, Seasonality, and Trend) model, and the results of this model were promising. It was concluded that 42% of the lands in the study area are vulnerable to the risk of meteorological drought, rivers permanently irrigate 37%, and 21% are cultivated in the winter season only.

1. Introduction

Risk assessment is a systematic procedure for assessing hazards' characteristics, probability, and magnitude linked to specific substances, situations, actions, or events while considering relevant ambiguity [1]. Risk refers to the possibility of adverse outcomes for human or environmental systems, and it is characterized by three essential elements: hazard, vulnerability, and exposure [2]. Land degradation is a risk with three basic components for risk assessment: hazard, the impact of global climate change; vulnerability, the exposure of bare land to the risk of degradation; and exposure, the direct impact on human life. Since land degradation is a complex problem [3], it will be a multi-hazard, where each of the most significant impacts that inevitably lead to degradation can be considered a hazard. One of the most critical factors in land degradation is drought in all its forms, especially in agricultural lands where drought is pivotal in exposing the cropland to degradation [4-5].

Drought is one of the five processes that lead to land degradation [4]. It is also described by its slow effect and recurrence according to severity and duration [6-7]. The risks of drought's impact lie in its effect on plant nutrients due to its effect on organic carbon. Drought also causes soil erosion due to winds and dust storms. In addition, the main danger to humans is the lack of cropland crops, food resources, and plant products.Drought is divided into four types: meteorological, agricultural, hydrological, and socioeconomic drought. The absence or severe decrease in rainfall during the rainy season over a specific area defines that it is suffering from a meteorological drought [8]. Meanwhile, the definition of agricultural drought is a lack of soil moisture and is a hazard, especially during the initial growth period of plant growth [3,9-10]. Building dams and controlling the course of the river, especially in the upstream countries, is considered one of the human interventions in creating drought, which is a type of socioeconomic drought [11]. Hydrological drought is a decrease in river water flow or groundwater reserves caused

http://doi.org/10.30684/etj.2025.155327.1855
Received 27 November 2024; Received in revised form 21 February 2025; Accepted 01 March 2025; Available online 24 March 2025
2412-0758/University of Technology-Iraq, Baghdad, Iraq

by climate change [12]. Meteorological drought is the most common and significant variety, as it frequently serves as the precursor to other drought forms [13].

Researchers paid close attention to the drought issue in Iraq, evaluating drought characteristics throughout the country using different methods and data. Israa et al. [14], attempted to evaluate agricultural drought overall in Iraq by examining the NDVI time series derived from MODIS, which has a spatial resolution of 250 meters. Youssef et al. [15], employed four distinct spectral drought indices to monitor agricultural drought in Iraq: the vegetation health index (VHI), the vegetation drought index (VDI), the visible and shortwave infrared drought index (VSDI), and the temperature-vegetation dryness index (TVDI). All indices were derived from the MODIS dataset of the Terra satellite, which has a spatial resolution of 250 meters. Imzahim et al. [5], used NDVI and the Vegetation Condition Index (VCI) obtained from Landsat 8 to monitor agricultural drought in the middle Euphrates Area. Lubna et al. [16], used NDVI derived from landsat 8 t and standardized precipitation index (SPI) from ground weather stations (GWSs) to monitor the agricultural and metrological drought in the Wasit Province. Zaidoon et al. [17], presented a methodology for integrating TRMM data with GMSs data through the SPI application to monitor the meteorological drought in the Western Iraq study area.

Previous studies have monitored and evaluated both meteorological and agricultural droughts. To our knowledge, no geostatistical model has been developed to identify agricultural lands vulnerable to the risk of meteorological drought, particularly in the Dhi Qar study area. This research aims to address this gap by presenting a geostatistical model that identifies agricultural lands vulnerable to metrological drought risk. The model will operate at the pixel level with a spatial resolution of 30 meters. The objectives of this research are as follows: (i)- Isolating the influence of the river on agricultural areas. In other words, to what extent can rivers be relied upon for irrigation in the wet season? (ii)- Identifying the areas vulnerable to metrological drought.

2. Materials and methods

2.1 Study area

This model was applied to the Dhi Qar Governorate in Iraq. Dhi Qar Governorate is a typical study area due to its environmental diversity, as it contains rivers, agricultural areas, pastures, marshes, and wetlands, see Figure 1. Dhi Qar governorate extends from Wasit governorate in the north to Basra governorate in the south and from Maysan governorate in the east to Al-Muthanna governorate in the west of Iraq. The study area is located between latitudes 30° and 32° North and longitudes 45° and 47° East. Dhi Qar governorate is approximately 161.5 km long and has a width ranging from 55 km to 142 km. The major rivers in Dhi Qar are the Gharraf River and the Euphrates River. Gharraf River originates from the Kut Dam. The Kut Dam is situated on the Tigris River. The Euphrates River also flows through the southwestern part of the governorate.

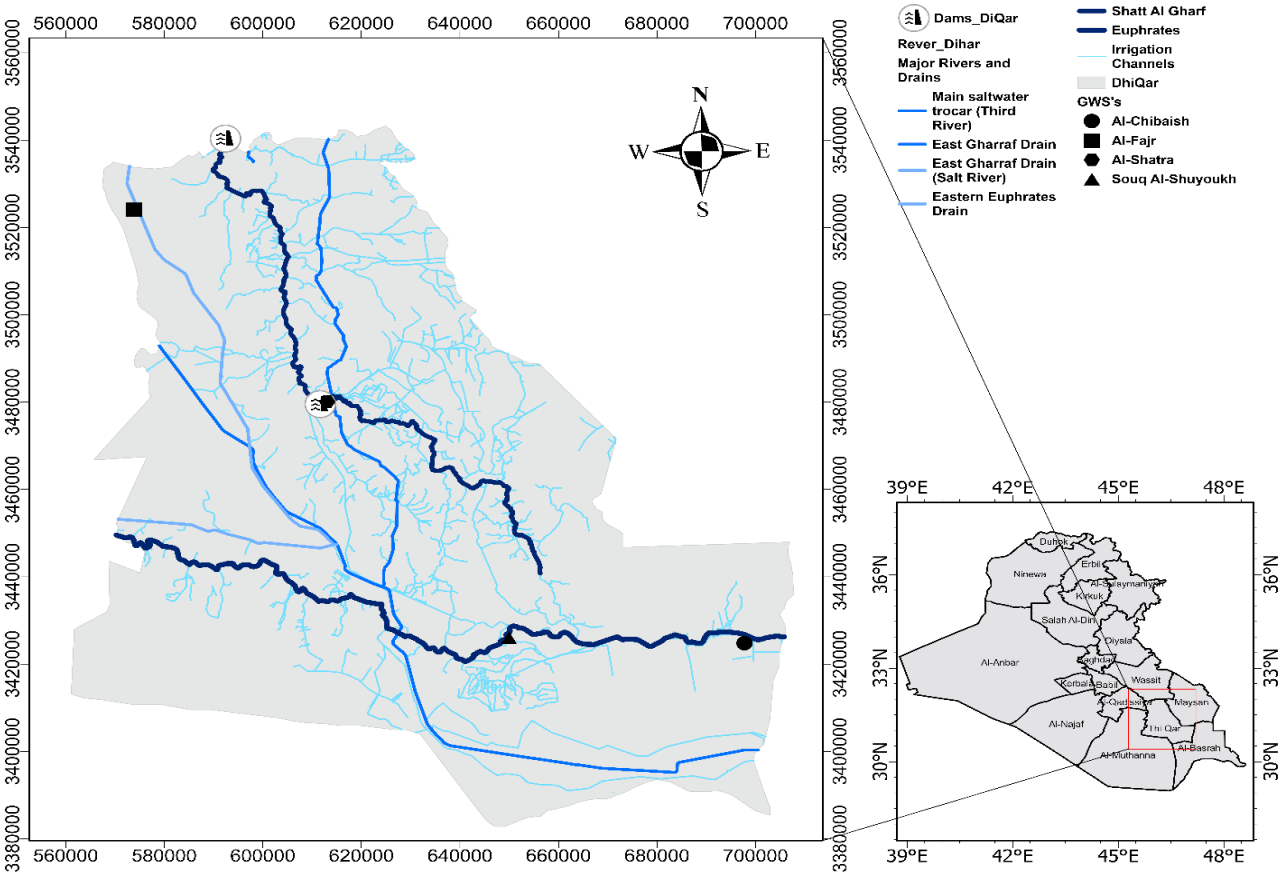

Figure 1: The study area

2.2 Data

Different data sources were utilized for our research, including rainfall amounts, land used/land cover (LULC), vegetation index, and moisture index (see Table 1). Rainfall data from ground weather stations (GWS) are more spatially accurate but less reliable than satellite data in terms of temporal accuracy and spatial distribution. The Dhi Qar study area has four GWSs: Al-Shtraa, Al-Fajr, Chibaish, and Souq Al-Shuyoukh (see Figure 1). These stations are poorly distributed in the study area, and there is also inconsistency in the time of observations and frequent malfunctions at different periods for each station. In our previous work, CHIRPS was chosen as the best alternative for rainfall data based on evaluating the quality of its data with the data of the four GWSs. CHIRPS covers parts of the world between 50° N and 50° S and has different spatial resolutions. The available spatial resolution is between 0.05° and 0.01° depending on the region and the period [18]. This dataset has been previously reported by Funk et al., [19].

Table 1: The data used, its source, and its abbreviation

Data	Abbreviation	Resolution	Time	Source
Rainfall Estimates from Rain Gauge and Satellite Observations	CHIRPS	500 m	2013-2023	https://data.chc.ucsb.edu/products/CHIRPS-2.0/
land used/land cover	LULC	10 m	2021	https://worldcover2021.esa.int/download
Normalized Difference Vegetation Index	NDVI-L8	30 m	2013-2024	Post-processing of Landsat satellite images, source https://earthexplorer.usgs.gov/
Normalized Difference Moisture Index	NDMI-L8			

Land cover/land use (LULC) data were collected from global ESA (European Space Agency) world cover. LULC data with a spatial resolution of 10 meters and overall accuracy 82..1 +/-1.0 in Asia [20-21].Compared with other global LULC products, ESA World Cover achieved the highest overall accuracy [22]. Landsat 8 data for the study area's red, blue, and thermal bands was downloaded from the United States Geological Survey (USGS). The data was used to extract NDVI and NDMI from 2013 to 2024.

2.3 Methodology

The research methodology involves creating a geostatistical model to understand the relationship between rainfall, vegetation cover, and moisture content. This model is then validated through ground truth data and field visits. Additionally, the time series of rainfall and NDVI are analyzed to confirm the relationship between rainfall and vegetation cover in the areas identified by the geostatistical model.

2.3.1 Geostatistical model development

Our geostatistical model explores the relationship between rainfall, vegetation cover, and moisture content. This hypothesis can be summarized as follows: (A weak relationship among humidity, vegetation cover, and rainfall suggests that a river influences the area, and vice versa). This hypothesis was tested over twelve years, from 2013 to 2024. Based on the hypothesis and with three determinants (rain, humidity, vegetation), the correlation is once between rain and the vegetation Index (NDVI-Rian) and another time between rain and the moisture Index (NDMI-Rian). There will be two possibilities: a strong correlation between NDVI-Rian and a strong correlation between NDMI-Rian (high-high correlation: H-H NDVI-Rain-NDMI).

The second possibility is the opposite of the first ((low-low correlation: L-L NDVI-Rain-NDMI). Accumulated rainfall data were collected from the beginning of the rainy season in October- November [23], to the start of March, and the time lag for collecting the NDVI and NDMI data was 20 days. Therefore, with the fixed time lag for collecting the NDVI-NDMI data in March, we will have a third possibility in our hypothesis (high-low correlation: H-L NDVI-Rain-NDMI). The third possibility indicates the presence of agriculture during the data collection period, which may indicate a strong correlation with NDVI-Rain and a weak correlation with NDMI-Rain. The second possibility is the presence of water and agriculture throughout the year (region of influence of rivers). The first possibility indicates the synchronization of agriculture with the abundance of water. Note Table 2 and Figure 2.

Table 2: Possible probabilities hypothesis for the geostatistical model

probability	Interpretation
H-H NDVI-Rain-NDMI	The relationship between water abundance and rainfall abundance
L-L NDVI-Rain-NDMI	The water source is constant (river effect), and water availability is not related to rainfall abundance.
H-L NDVI-Rain-NDMI	The effect of time lag.

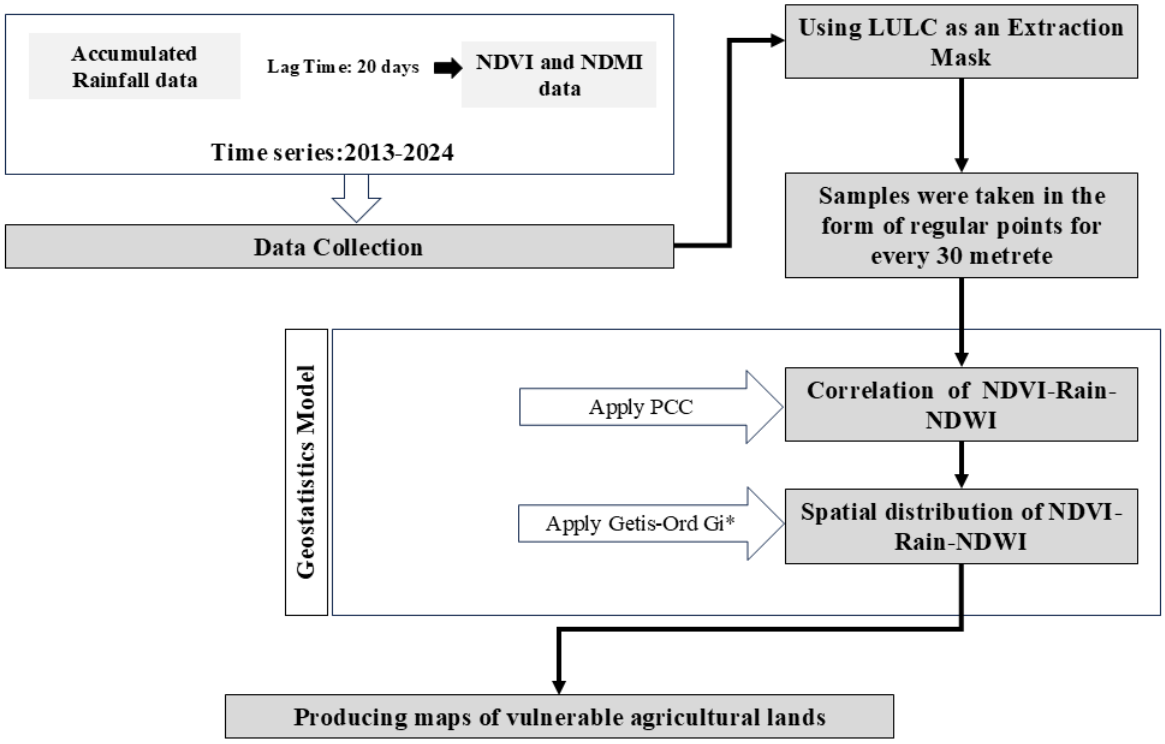

Figure 2: Explains the methodology of Geostatistical model development

Personal Correlation Coefficient (PCC) is applied to find the relationship between vegetation index, moisture content, and rainfall. PCC is a global spatial statistical test that examines the linear relationship between two variables [24]. It is calculated for each pixel representing the agricultural lands using Equation 1:

$$PCC(x,y) = \frac{\sum_{i=1}^{n}(x_i - \ddot{x})(y_i - \dot{y})}{\sqrt{\sum_{i=1}^{n}(x_i - \ddot{x})^2 \sum_{i=1}^{n}(y_i - \dot{y})^2}} \quad (1)$$

The values of x and y are the first and second variables, respectively, and in the case of our geostatistical model, x will be the value of the NDVI and NDMI, and y will be the value of the amount of rainfall for pixel i. PCC has been used in many studies to find the relationship between climate elements and ecosystem elements [25-27]. Paul et al. [28], used PCC to analyze the relationships between parameters, including mean annual temperature, annual rainfall, NDVI, night light, distance from water, human population density, and elevation. They applied this data to investigate the habitation patterns of deer in northern India. In another study, Ferro et al. [29], employed PCC to identify correlations between NDVI and quantitative and qualitative parameters of vines. Similarly, Feizabadi et al. [30], Utilized PCC to find correlations among various parameters such as the Digital Elevation Model (DEM), NDVI, human influences, annual mean temperature (°C), and annual precipitation (mm). Hua et al. [31], used PCC to assess the correlation between estimated slopes, annual changes in phenology, and different climatic factors. Lastly, Sannigrahi et al. [32], applied PCC to establish correlations between multiple parameters to study the impacts of climate change and land use dynamics on the biophysical and economic values of ecosystem services in a nature reserve area. These parameters included vegetation indices, climate data (e.g., evaporation, precipitation, temperature), DEM, soil data, roads, railways, and other relevant data for their study.

The value of PCC is between a negative one and a positive one, where a positive one indicates a strong correlation value, a negative one indicates an inverse correlation value, and zero indicates no correlation between the parameters. The parameters of the geostatistical developer model are rainfall from CHIRPS, NDVI, and NDMI extracted from Landsat 8 (Equations 2 and 3). Samples measuring 30 m x 30 m were collected from agricultural lands and extracted from the LULC layer, (see Figure 2). Next, classify each pixel containing a PCC value using the Getis-Ord Gi* statistical index.

$$NDVI = \frac{NIR - Redband}{NIR + Redband} \quad (2)$$

$$NDMI = \frac{NIR - SWIR1}{NIR + SWIR1} \quad (3)$$

The Getis-Ord Gi* statistical index provided a better understanding of the relationship between vegetation, humidity, and rainfall in agricultural lands where the river is used as a source of irrigation. The statistical significance of the hot spot analysis was tested using the standardized Z-value, with higher positive Z-values indicating tighter clustering of high values (hot spots) and lower negative Z-values indicating tighter clustering of low values (cold spots). It has been utilized in spatial analysis for

ecosystem and ecological environmental studies [33-37], natural hazards [38-39], flood studies [40-41], health and population patterns [42-43], and drought [44-46]. This study used the Getis-Ord Gi* index to investigate the clustering of high and low correlation of the vegetation, humidity, and rainfall (NDVI-Rain and NDMI-Rain) in the study area from 2013 to 2024. Its mathematical formula is as follows (From Equation 4 to 6):

$$G^* = \frac{\sum_{j=1}^{n} w_{i,j} x_j}{\sum_{j=1}^{n} x_j} \tag{4}$$

$$Z(G^*) = \frac{\sum_{j=1}^{n} w_{i,j} x_j - \mathcal{X} \sum_{j=1}^{n} w_{i,j}}{S\sqrt{\frac{\left[n\sum_{j=1}^{n} w_{i,j}^2 - \left(\sum_{j=1}^{n} w_{i,j}\right)^2\right]}{n-1}}} \tag{5}$$

$$S = \sqrt{\frac{\sum_{j=1}^{n} x_j}{n} - \mathcal{X}^2} \tag{6}$$

where G* is the clustering index of pixel i, Wi,j is the weight matrix between pixel i and j (calculated based on the Euclidean distance between pixel), x,j is the attribute value of a pixel, n is the total number of pixel, χ is the mean of all pixel's attributes within the study area, and S denotes the standard deviation of all pixel's attribute values. In our model, each pixel's attribute value was considered the PCC value of NDVI-Rain and NDMI-Rain.

2.3.2 Model validation

The geostatistical model is validated in two ways. The first is a field visit that includes photographing and interviewing the landowners. The questions are typically answered with short responses, such as "When was the last planting season?" and "Is groundwater used for irrigation?" (refer to Table 3). The second method to achieve this is to analyze the time series of rainfall and vegetation index using the BEAST (Bayesian Estimator of Abrupt Change, Seasonality, and Trend) model.

Table 3: Ground truth sample questions

E =xxxxxx **N=xxxxxxx UTM Zone:38N ID=1**		**Additional comment**
What is the source of irrigation?	*********	**********
Cultivation season (winter, summer, mixed)?	*********	**********
Do you use groundwater for crop cultivation?	*********	**********
During the past ten years, has the planting season been regular?	*********	**********
What year was the last planting season?	*********	**********
Which year was the most abundant in water resources?	*********	**********
What year is considered the driest?	*********	**********

BEAST decomposes the time series into its trend, seasonal, and remainder components. However, the model structure, or the number and timing of breakpoints, is estimated through Bayesian modeling to reduce uncertainty, overfit, and model misspecification. This model was formulated by John Zhao et al. [47]. The BEAST model was used with remote sensing data for time series analysis [48-52]. Many other studies in various fields, for example, in ecology [53], environmental engineering [54], in biomedical engineering [55], geography [56], and watershed hydrology [57]. The power of the BEAST model is in revealing the local trend between periods, giving the added benefit of a reasonable interpretation of vegetation-rain change in the study area. BEAST formulated are:

$$Y_t = T(t_i; \Theta_T) + S(t_i; \Theta_s) + \varepsilon_i \tag{7}$$

where Y is the observed data at time t (t = 1, …n), i is the index of the time dimension, T is the trend component, and it is a piecewise linear model with m breakpoints and m + 1 linear models, where abrupt changes are found at the breakpoints τi (i = 1, …m), and gradual changes are given by the:

$$T = \alpha, + \beta_i \mathrm{t} \tag{8}$$

S is the seasonal component that fits with a harmonic model with ρ breakpoints and ρ + 1 harmonic models, where seasonal changes are found at the breakpoints ξj (*j* = 1, … ρ). Harmonic models account for periodicity using *K* harmonic terms (sinusoids with different characteristics):

$$S_i = \sum_{k=1}^{k} \varphi_{j.k} \sin\left(\frac{2\pi k t}{f} + \delta_{j,k}\right) \tag{9a}$$

for $\xi j\text{-}1 \leq t < \xi j$ and where φ is the amplitude, f is the frequency, and δ is the phase of the sine wave. The Equation 9 has been modified to be compatible with BEAST for handling non-linear time series such as the Rainfall and NDVI time series:

$$S_i = \sum_{k=1}^{k} \left[\gamma_{j.k} \sin\left(\frac{2\pi kt}{f}\right) + \theta_{j.k} \cos\left(\frac{2\pi kt}{f}\right)\right] \quad (9b)$$

where the linear coefficients of the regression model are γj,k = φj,kcosδj,k and θj,k = φj,ksinδj,k. Note that K is a user-defined constant (it does not vary across j segments). ε_i is the remainder component. The trend component linear model: ΘT represents the parameters related to the trend, and Θ_S represents the parameters related to seasonality. It is expressed in the following Equations:

$$\Theta_T = \{m\} \cup \{\tau_I\}_{i=1,\ldots..m} \cup \{\alpha, \beta_i\}_{i=0,\ldots.m} \quad (10)$$

$$\Theta_s = \{p\} \cup \{\xi\}_{j=1,.p} \cup \{k\}_{j=0,..p} \cup \{\gamma_{j,k}, \theta_{j,k}\}_{j=0,.p;k=1.,k_j} \quad (11)$$

Reformulating Equation7 as a simple linear regression:

$$Y_t = X_M(t_i)\beta_m + \varepsilon_i \quad (12)$$

where X_M is the design matrix with the form dependent on M, and M is where M is the model structure from Equations 10 and Equation 11:

$$M = \{m\} \cup \{\tau_I\}_{i=1,\ldots..m} \cup \{p\} \cup \{\xi\}_{j=1,\ldots.p} \cup \{k\}_{j=0,\ldots.p} \quad (13)$$

And β_m are the corresponding coefficients from Equations 10 and 12:

$$\beta_M = \{\alpha, \beta_i\}_{i=0,\ldots.m} \cup \{\gamma_{j,k}, \theta_{j,k}\}_{j=0,\ldots.p;k=1.,\ldots.k_j} \quad (14)$$

After preparing the necessary data and libraries, this model was implemented using the Google Colab platform. The library that contains the code for this model is Rbeast [58]. The full description of the BEAST model can be found in [47].

3. Results and discussion

3.1 Geostatistical model development

Approximately 5,500,000 pixels representing agricultural areas were extracted for the study area. Each pixel extracted from the LULC contains three values. The first and second values represent the NDVI and NDMI extracted from Landsat 8, and the third value represents the rainfall extracted from CHIRPS. The five million pixels were analyzed using the Getis-Ord Gi* statistical index. They were clustered based on their PPC values, with low correlation clusters in blue and high correlation clusters in red. The confidence levels were also indicated, with 99%, 95%, and 90% confidence levels displayed for each color gradient, see Figure 3 (a and b). Only each pixel value with a high correlation at a 99% confidence level was extracted, ignoring the other pixels with a lower confidence level.

The extension of the PCC-NDVI-Rain and PCC-NDMI-Rain regions is nearly identical. We observe that the L-L NDVI-Rain-NDMI region is close to the main rivers (Graff and Euphrates) with a confidence level of 99%. These regions exhibit a low correlation between moisture content and vegetation cover with the amount of rainfall. The L-L NDVI-Rain-NDMI region encompasses approximately 1600000 pixels and covers an area of 147890 hectares. According to our model, this area heavily depends on river water as a source of irrigation. The mean value of PCC is about 0.12 between rainfall and the NDMI and 0.24 between rainfall and NDVI in the L-L NDVI-Rain-NDMI region at a confidence level of 99%, see Figure 4a.

In contrast, the results indicate that the H-H NDVI-Rain-NDMI region is located farthest from the main rivers in the study area, covering approximately 19000000 pixels and an area estimated at 171900 hectares (see Figure 3c). The mean value of PCC is about 0.46 between rainfall and the NDMI and 0.52 between rainfall and NDVI in the H-H NDVI-Rain-NDMI region at a confidence level of 99% (see Figure 4b). Notably, the H-H NDVI-Rain-NDMI region covers a larger area than the L-L NDVI-Rain-NDMI region, with an increase of 7.5%. As previously assumed, vegetation cover and moisture content in the H-H NDVI-Rain-NDMI region are linked to water availability due to abundant rainfall. In contrast, the H-L NDVI-Rain-NDMI region results from the data collection lag time.

The H-L NDVI-Rain-NDMI region is mainly located between the L-L NDVI-Rain-NDMI region and the H-H NDVI-Rain-NDMI region (Figure 3c), covering 980000 pixels and about 87800 hectares. The mean value of PCC is about 0.41 between rainfall and the NDVI and 0.21 between rainfall and NDMI in the H-L NDVI-Rain-NDMI region at a confidence level of 99%, see Figure 4c. The H-L NDVI-Rain-NDMI region represents 21% of the total agricultural land. In comparison, the L-L NDVI-Rain-NDMI and H-H NDVI-Rain-NDMI regions represent 37% and 42% of the total agricultural land, respectively.

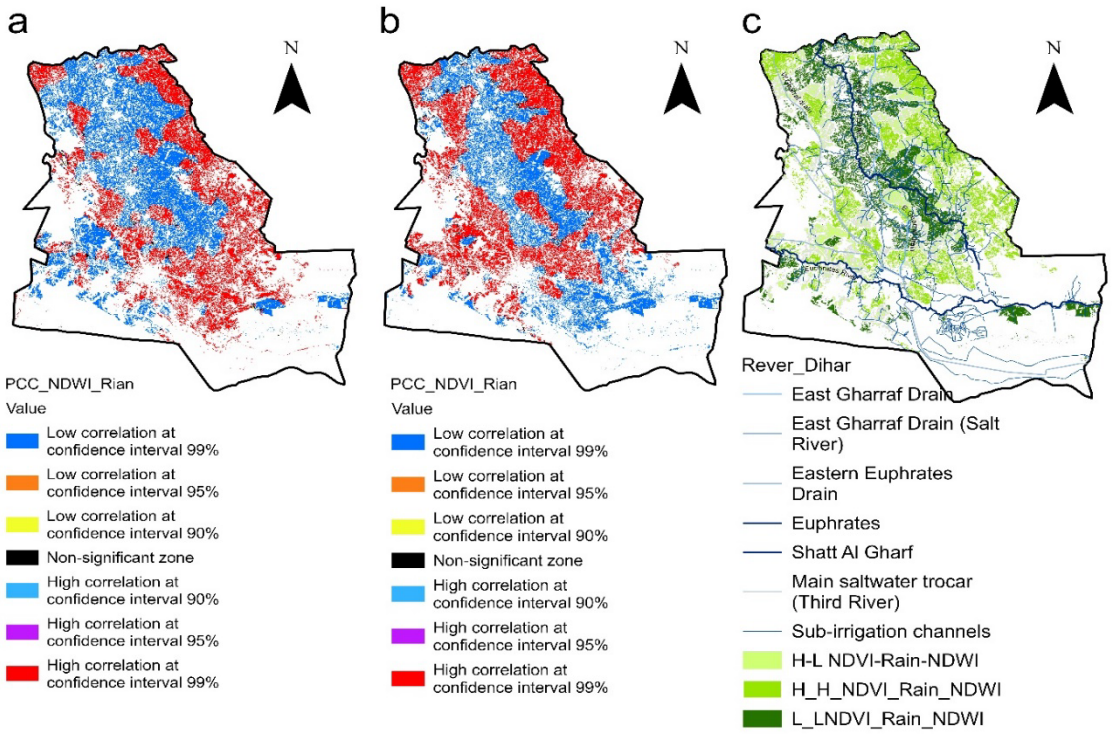

Figure 3: a and b Spatial distribution of PCC NDMI-Rainfall and PCC NDVI-Rainfall, respectively. c- show the H-L, H-H, and L-L regions

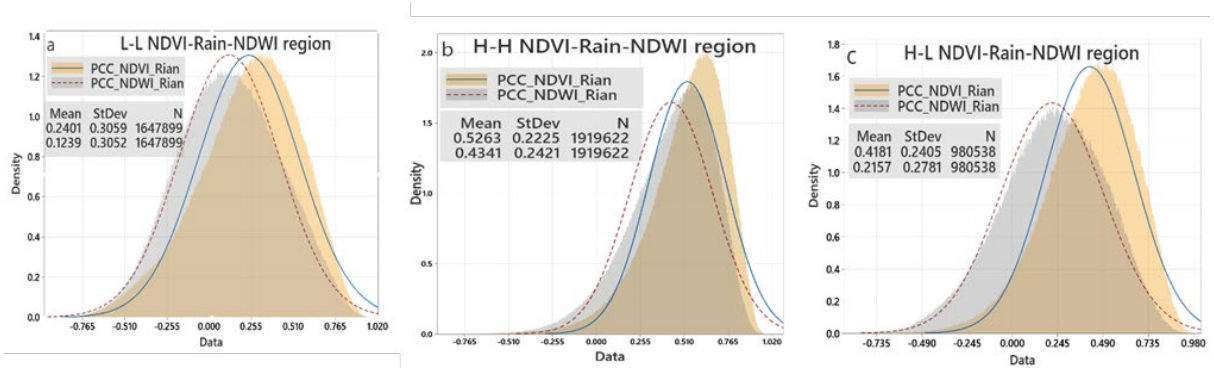

Figure 4: Frequency distribution chart a.L-L region, b.H-H region, and c-H-L region

3.2 Geostatistical model validation

3.2.1 Field verification

The field visit was conducted to verify the geostatistical developer model, which included interviewing the landowners and asking them questions. The questions were short answers arranged according to Table 2. We conducted around 20 interviews and collected 152 ground truth samples from various locations within the study area. All the landowners confirmed that rivers are the only source of irrigation and that wells are not used for crop irrigation. Wells were used daily to water some trees and quench their animals in areas facing severe water shortages, which they noticed in H-H NDVI-Rain-NDMI regions(refer to Figure 5a.4 and for more details, see Supplementary Materials No. 1). They also agreed that 2021-2022 was a dry year. Additionally, we observed a significant decrease in the water level in the irrigation canals, with the water barely reaching the bottom of the control gates. This can be seen in Figure 5a.2, b.1, and Supplementary Materials No. 1, which includes Image IDs 34, 44, 45, 56, 57, 68, 6981, 78, 93, and 121. These gates regulate water transfer from the L-L NDVI-Rain-NDMI regions to H-H NDVI-Rain-NDMI regions. This confirms that our model effectively identified and isolated areas affected by rainfall and the river. It is worth noting that all ground truth samples were collected in September and the beginning of October, before the rainy season, confirming that H-H NDVI-Rain-NDMI regions rely on the irrigation canals' water level during the rainy season. We also observed that landowners in L-L NDVI-Rain-NDMI regions and H-L NDVI-Rain-NDMI regions utilize pumps to lift water from the irrigation channels to their lands during irrigation. These pumps are either electric or use kerosene (see Figure 5 c.2,d. one and Supplementary Materials No. Image ID 5, 22, 110 and 116). It was also noted that most of the land in the H-H NDVI-Rain-NDMI regions was abandoned by farmers, as the farming process was no longer economically viable (see Supplementary Materials No. Image ID 16-21,64-73,94-94,105,135,149,150 and 151). This led to the growth of harmful plants see Figure 5 a.1,c.1, and c4. Finally, during our field visit, we noticed that the H-L NDVI-Rain-NDMI regions are cultivated in only one

season. These areas are cultivated in the winter season, specifically in November, with wheat and barley crops (see Image ID 6-10, 26-29, 36-49, 58-61, 83-85, 89-92 and 117-120 in Supporting Material No.1 where farmers prepare the land in October for the winter planting season). They are harvested in May and reach their maximum greenness in March.

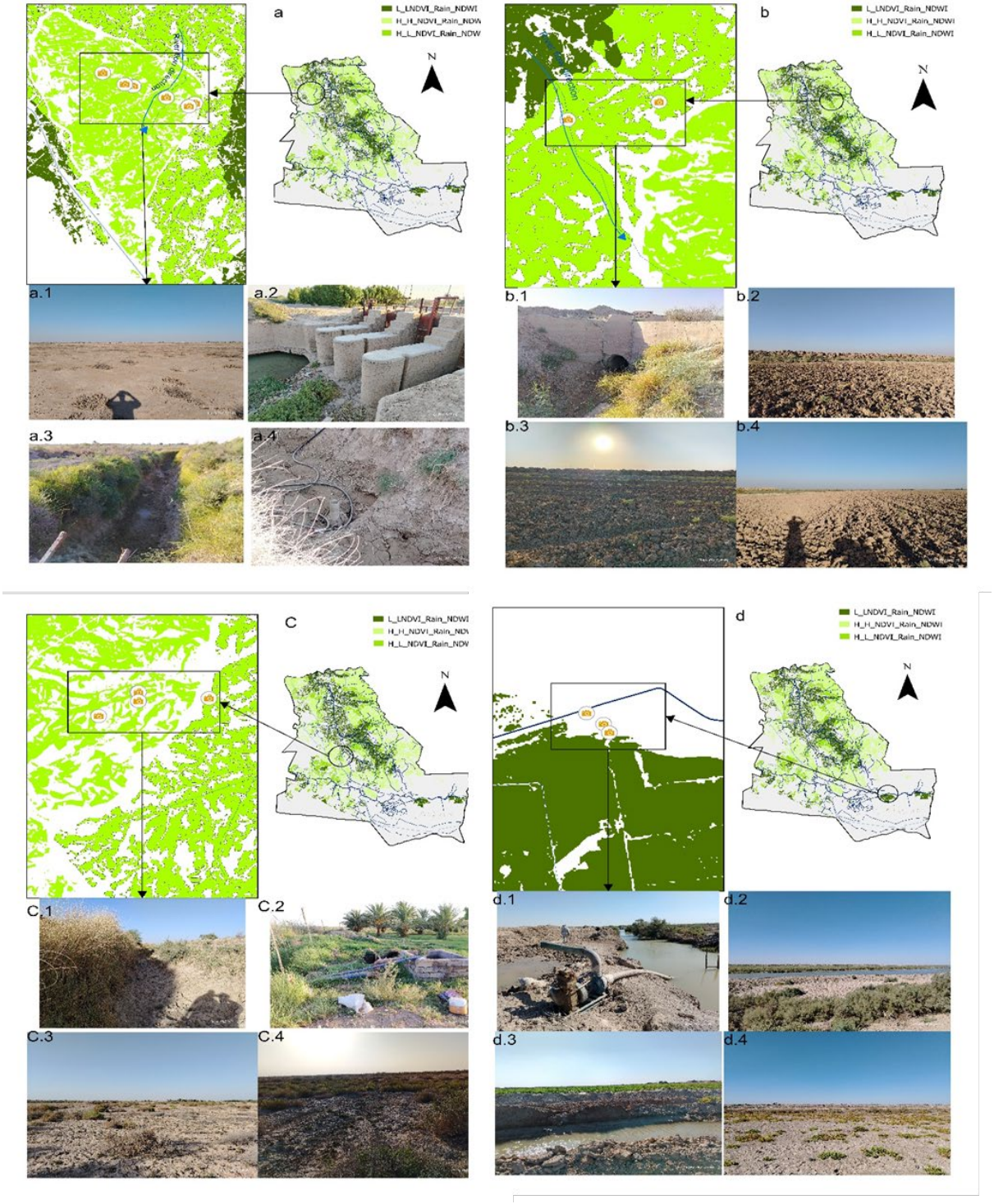

Figure 5: Ground truth samples

3.2.2 Time sires analysis

During the time series 2013-2024, the study area experienced significant fluctuations in rainfall amounts. The maximum recorded rainfall was 79 mm in 2019, while the minimum was 30 mm in 2021. The monthly average rainfall was approximately 25-30 mm during the rainy season, see Figure 6. The BEAST model's results include detecting seasonal and trend change points. Each change point identified over time in the season or trend was assigned a rank based on the Probability of Change Point (PCP) and the Probability of Change Point in this trend (PCPT). Refer to Table 4 for details.

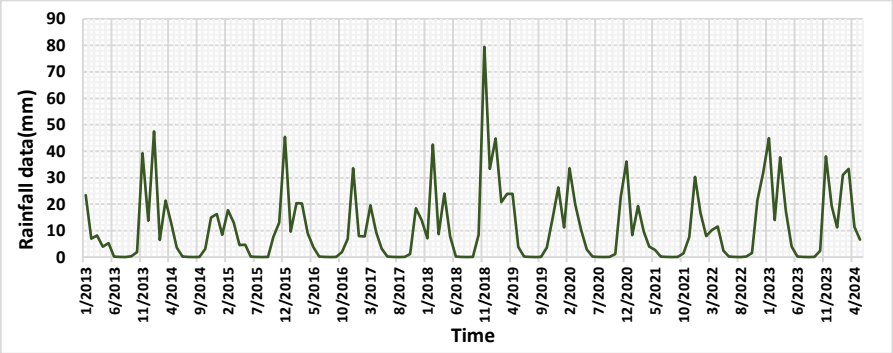

Figure 6: Monthly rainfall during the time series 2013-2024

The BEAST model's findings revealed ten seasonal change points during the rainy season, with PCP values ranging from 0.98 to 0.70. The highest PCP value from the previous season was recorded in October 2018 at 0.98. Additionally, between 2017 and 2018, there was a noticeable increase in rainfall amounts in 2018 compared to 2017, with a PCP of 0.97. The Trend Component (TC) in rainfall between the 2017, 2018 and 2019 seasons showed an upward trajectory, as the PCPT was estimated to be very high at 0.98 see Table 3 and Figure 7a. From October 2013 to 2014, no significant changes were observed in the rainy season. The first change was recorded in January 2015, with a PCP of 0.87. The TC of rainfall remained stable without significant increases until January 2017, with PCP values recorded at 0.82 and a notably low value of 0.019 for 2016. This indicates no change in the amount of rainfall during 2016. Throughout these years, the PCPT was around 0.44. A similar pattern emerged in April 2019 when the trend began to decline, with the PCPT value to approximately 0.60, confirming the decrease in rainfall for that year. This decline persisted until October 2022, when the region observed increased rainfall amounts following that period see Figure 6 and Figure 7a. To summarize the above, we notice that from 2013 to 2014, there was a steady TC in rainfall amounts, with a slight increase in the 2015-2016 season. Then, we notice a decline in the TC of rainfall amounts in the 2017-2018 season, followed by a significant increase in the TC of rainfall amounts in the 2018-2019 season. This TC increased for just one season, but then there was a significant decline in rainfall amounts in the 2019-2020 season. This substantial decline continues until 2022, followed by a slight increase in 2023. This increase continues until 2024.

The H-H region experienced fluctuations in seasonal values of NDVI over the time series from 2013 to 2024. During this period, nine seasonal change points were recorded, confirmed by PCP values ranging from 0.999 to 0.925. The highest ranking occurred in January 2019, while the lowest was in October 2016. In April 2020, the PCP value was 0.71, lower than other PCP values in the H-H region but still considered high. Five trend change points were identified in the H-H region, with PCPT values between 1 and 0.95. The highest trend change point, recorded in October 2018, had a PCPT value of 1. Trend change points followed this in September 2021, January 2023, September 2014, and October 2019, with PCPT values of 0.999, 0.996, 0.967, and 0.953, respectively. The positive TC observed in October 2018 marked the beginning of increased water abundance due to heavy rainfall. They exhibited the highest slope in TC throughout the 2013-2024 time series. In contrast, the negative TC from September 2021 to January 2023 reflected a significant decline, characterized by sharp fluctuations in the NDVI value. These fluctuations were closely related to occurrences of abundant rainfall see Table 3 and Figure 7b.

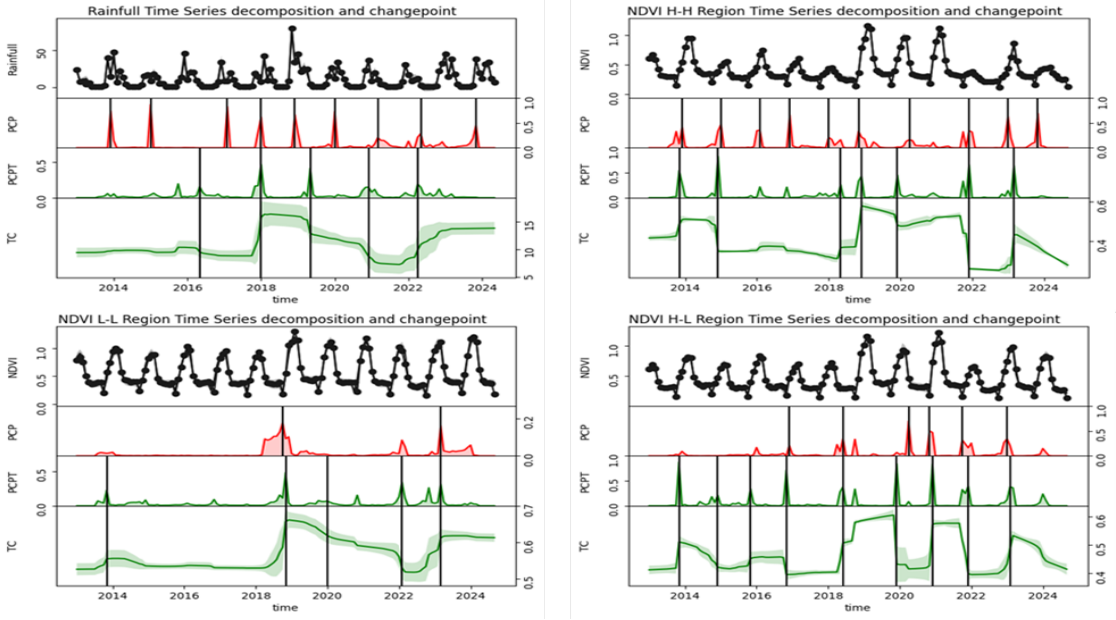

Figure 7: Time Series decomposition and changepoint for a-rainfall, b-H-H region, c-L-L region, and d-H-L region

Table 4: Shows that the BEAST model's results include detecting seasonal and trend change points for rainfall, H-H, L-L, and H-L regions

Rain full						**H H Region**					
S.C.P			***T.C.P***			***S.C.P***			***S.C.P***		
Rank	***Time***	***PCP***	***Rank***	***Time***	***PCPT***	***Rank***	***Time***	***PCPT***	***Rank***	***Time***	***PCPT***
1	Oct-18	0.985	1	Jan-18	0.830	1	Jan-19	0.999	1	Oct-18	1.000
2	Jan-18	0.973	2	Oct-20	0.652	2	Sep-21	0.998	2	Sep-21	0.999
3	Jan-20	0.883	3	Apr-19	0.601	3	Sep-13	0.986	3	Jan-23	0.996
4	Jan-15	0.878	4	Apr-22	0.466	4	Jan-23	0.984	4	Sep-14	0.967
5	Oct-13	0.875	5	Apr-16	0.441	5	Oct-23	0.976	5	Oct-19	0.953
6	Oct-23	0.841	6	Sep-15	0.312	6	Jan-18	0.959	6	Apr-13	0.883
7	Jan-17	0.823	7	Jan-15	0.204	7	Sep-14	0.958	7	Jan-18	0.351
8	Jan-21	0.726	8	Oct-13	0.183	8	Jan-16	0.928	8	Jan-22	0.297
9	Mar-22	0.710	9	Jan-20	0.111	9	Oct-16	0.925	9	Jan-16	0.130
10	Jan-16	0.019				10	Apr-20	0.718	10	Oct-16	0.107
L L Region						**H L Region**					
S.C.P			***S.C.P***			***S.C.P***			***S.C.P***		
Rank	***Time***	***PCP***	***Rank***	***Time***	***PCPT***	***Rank***	***Time***	***PCP***	***Rank***	***Time***	***PCPT***
1	Sep-18	0.826	1	Oct-18	0.972	1	Sep-21	0.926	1	Apr-18	1.000
2	Jan-23	0.304	2	Jan-23	0.793	2	Mar-20	0.917	2	Jan-23	0.981
3	Jan-22	0.266	3	Jan-22	0.606	3	Apr-18	0.897	3	Sep-21	0.970
4	Apr19	0.123	4	Oct-13	0.441	4	Oct-22	0.812	4	Oct-13	0.933
5	Jan-14	0.118	5	Jun-14	0.373	5	Mar-19	0.573	5	Sep-14	0.799
6	Oct-20	0.059	6	Oct-19	0.341	6	Oct-20	0.518	6	Jan-24	0.650
7	Jan-16	0.056	7	Oct-20	0.241	7	Oct-16	0.515	7	Jan-16	0.641
8	Apr-17	0.039	8	Oct-16	0.168	8	Jan-13	0.181	8	Oct-19	0.581
9	Mar-15	0.017	9	Jan-24	0.151	9	Jan-24	0.113	9	Oct-20	0.554
			10	Jan-16	0.110	10	Sep-17	0.031	10	Oct-15	0.467

Note: S.C.P (Seasonal Change Points), T.C.P(Trend Change Points), PCPT(Probability of Change Point), and PCPT (Probability of Change Point in this trend).

The L-L region exhibited stability, with nine seasonal change points identified. These seasonal change points were minimal, with the highest occurring in September 2018, when the PCP value was 0.826. In October 2018, the positive TC sharply increased, reaching a PCPT value of 0.972. However, a significant negative TC was observed in January 2022, with the PCPT value dropping to 0.60. In addition to the changes noted in the previous paragraph, the L-L region recorded eight seasonal and nine trend change points. The probability associated with these changes was weak, with PCP values ranging from 0.266 to 0.017 and PCPT values between 0.606 and 0.110. This suggests that the NDVI values remained stable and did not directly correlate with rainfall amounts, see Table 3 and Figure 7c.

The H L region recorded ten seasonal change points, comprising four highly probable and six low probable occurrences. The most significant change point was observed in September 2021, followed by March 2020, April 2018, and October 2022, with PCP values of 0.926, 0.917, 0.897, and 0.812, respectively. The remaining seasonal change points were associated with lower probability, showing PCP values of 0.537, 0.518, 0.515, 0.181, 0.0131, and 0.031, occurring in March 2019, October 2020, October 2016, January 2013, January 2024, and September 2017, respectively. Additionally, this region experienced ten trend change points, with the highest ranking in October 2018, with the PCPT value reaching 1. The other nine trend change points had values ranging from 0.90 to 0.46, occurring in January 2023, September 2023, October 2013, September 2014, January 2024, January 2016, October 2019, October 2020, and October 2015, with PCPT values of 0.981, 0.970, 0.933, 0.799, 0.650, 0.641, 0.581, 0.554, and 0.467, respectively. The trend change point in April 2018 was a positive TC, while the trend change point in September 2021 was negative. The trend changes coincided with variations in rainfall, suggesting a connection between the H L region and the rainy season.

To summarize, the H-H region experienced significant fluctuations in NDVI values that were closely aligned with changes in rainfall amounts in the study area. In contrast, the L-L region exhibited stable NDVI values without fluctuations during the time series from 2013 to 2024. The H-L region also experienced fluctuations, but they were less pronounced than those in the H-H region.

3.3 Discussion

The geostatistical developer model has identified an agricultural region that relies heavily on the Gharraf River, with farming extending approximately 10 to 20 kilometers on either side of the river. This area encompasses about 190000 hectares. In contrast, smaller regions that depend on the Euphrates River support continuous agriculture. However, they are significantly less extensive, covering an area of about 53,000 hectares, as illustrated in Figure 3c. The agricultural lands surrounding the Gharraf River, classified as the (L-L) region, are notably more extensive than those primarily dependent on the Euphrates River. This difference can be attributed to the varying characteristics of the Euphrates River during the rainy season, as observed by Ali and Jabbar [59-60]. Most agricultural areas near the Euphrates River fall within the (H-L) region. This observation further reinforces the effectiveness of our model in identifying agricultural areas that rely on rivers.

Comparing the H-H region and the (L-L) region, the (H-H) region is approximately 7% larger in area than the L-L region. The (H-H) region is sensitive to water availability due to the abundance of rain and is vulnerable to meteorological drought. Hassan et al. [61], confirmed this result in their research, confirming that 80% of agricultural areas are threatened by desertification.

A time series analysis of rainfall in the study area revealed a significant decrease. Kazim et al. [62], also reported similar findings in their research. The years experiencing the most substantial deficits were the 2016-2017 and 2021-2022 seasons. Several researchers confirm these observations, indicating that meteorological droughts occurred across Iraq during the 2016-2017 and 2021-2022 periods [5,63-64]. This evidence supports the conclusion that the study area is affected by global climate change.

Applying the BEAST model to analyze time series data provided a more comprehensive understanding of rainfall patterns in the Dhi Qar region. We identified two significantly wetter seasons compared to previous years. The first season was from 2018-2019, marked by an increase in TC, while the second occurred following a severe dry period in 2021, specifically during the 2022-2023 season. A notable similarity between these two seasons is their onset; both began with a change in TC in October. This finding aligns with the work of Adnan [23], who confirmed that wet seasonal characteristics are linked to their October start, (see Figure 7a). This analysis enhances the credibility and effectiveness of the BEAST model in detecting changes in seasonal and trend components. Consequently, integrating field visits with time series analysis using the BEAST model strengthens our geostatistical model for identifying and isolating regions affected by the river (L-L region), areas vulnerable to meteorological drought (H-H region), and regions that exhibit commonality with lag time (H-L region). H-L regions are areas that are cultivated only in the winter season.

4. Conclusion

The geostatistical model effectively differentiates agricultural lands in Dhi Qar Governorate that rely on rivers for permanent irrigation from those cultivated seasonally or depend on rainfall for their water supply. Our model revealed that agricultural lands dependent on the Gharraf River extend 10 to 20 kilometers on both sides. In contrast, the areas reliant on the Euphrates River extend shorter distances. Additionally, the agricultural lands that depend on rainfall are extensive, reaching the edges of the study area. Based on our findings, we concluded that 42% of the agricultural land in the study area is vulnerable to meteorological drought. Furthermore, 37% of these lands rely on rivers for irrigation and are cultivated for multiple seasons. In comparison, 21% are cultivated for only one season each year. We also reached the following secondary conclusions:

- Although irrigation canals extend from the main rivers, they are outdated and inefficient in delivering water to distant locations. This issue has been exacerbated by unsustainable water usage and inadequate water management.
- Most agricultural lands near the Euphrates River are only cultivated in the winter when there is abundant water from heavy rains. This is due to the characteristics of the Euphrates River water, which experiences high salinity in both the dry and summer seasons.
- The BEAST model has demonstrated its effectiveness in time series analysis by accurately identifying seasonal, trend, and cyclic component changes. Combining the BEAST model with a geostatistical approach yielded promising results in spatiotemporal analysis.

Author contributions

Conceptualization, **M. Azeez**, **H. Al Sharaa**, and **A. Ziboon**; data curation, **M. Azeez**; methodology, **M. Azeez**; software, **M. Azeez**; supervision, **H. Al Sharaa**, and **A. Ziboon**; validation, **M. Azeez**, **H. Al Sharaa**, and **A. Ziboon**; visualization, **M. Azeez**; writing—original draft preparation, **M. Azeez**; writing—review and editing, **H. Al Sharaa**, and **A. Ziboon**. All authors have read and agreed to the published version of the manuscript.

Funding

This research received no specific grant from any funding agency in the public, commercial, or not-for-profit sectors.

Data availability statement

The data that support the findings of this study are available on request from the corresponding author.

Conflicts of interest

The authors declare that there is no conflict of interest.

References

[1] SHARMA, Jagmohan; RAVINDRANATH, Nijavalli H. Applying IPCC 2014 framework for hazard-specific vulnerability assessment under climate change. Environ. Res. Commun., 1 (2019) 1-7. https://dx.doi.org/10.1088/2515-7620/ab24ed

[2] H. Guo, X. Wen, Y. Wu, J. Wang, and Q. Liang, Drought risk assessment of farmers considering their planting behaviors and awareness: A case study of a County from China, Ecol. Indic., 137 (2022) 108728. https://doi.org/10.1016/j.ecolind.2022.108728

[3] R. S. Dwivedi, Geospatial technologies for land degradation assessment and management. CRC. Press., 2018.

[4] R. Prăvălie, Exploring the multiple land degradation pathways across the planet, Earth Sci. Rev., 220 (2021) 103689. https://doi.org/10.1016/j.earscirev.2021.103689

[5] I. Alwan, A. R. Ziboon, and A. Khalaf, Monitoring of Agricultural Drought in the Middle Euphrates Area, IraqUsing Landsat Dataset, Eng. Technol. J., 37 (2019) 222-226. https://doi.org/10.30684/etj.37.7A.1

[6] D. Ge, X. Gao, and W. Xinguang, Changes in spatiotemporal drought characteristics from 1961 to 2017 in northeastern maize-growing regions, China, Irrig. Sci., 42 (2024) 163-177. https://doi.org/10.1007/s00271-023-00893-4

[7] A. Fathi, H. Shafizadeh-Moghadam, M. Minaei, and T. Xu, Influence of drought duration and severity on drought recovery period for different land cover types: evaluation using MODIS-based indices, Ecol. Indic., 141 (2022) 109146. https://doi.org/10.1016/j.ecolind.2022.109146

[8] A. A. Belal, H. R. El-Ramady, E. S. Mohamed, and A. M. Saleh, Drought risk assessment using remote sensing and GIS techniques, Arabian J. Geosci., 7 (2014) 35-53. https://doi.org/10.1007/s12517-012-0707-2

[9] V. Sehgal, N. Gaur, and B. Mohanty, Global Flash Drought Monitoring Using Surface Soil Moisture, Water Resour. Res., 57 (2021) 1-25. https://doi.org/10.1029/2021WR029901

[10] S. Chen, T. Y. Gan, X. Tan, D. Shao, & J. Zhu, Assessment of CFSR, ERA-Interim, JRA-55, MERRA-2, NCEP-2 reanalysis data for drought analysis over China, Clim. Dyn., 53 (2019) 737-757. https://doi.org/10.1007/s00382-018-04611-1

[11] R. Albarakat, M.-H. Le, and V. Lakshmi, Assessment of drought conditions over Iraqi transboundary rivers using FLDAS and satellite datasets, J. Hydrol Reg. Stud., 41 (2022) 101075. https://doi.org/10.1016/j.ejrh.2022.101075

[12] Y. Tramblay, A. Koutroulis, L. Samaniego, S. M. Vicente-Serrano, F. Volaire, et al., Challenges for drought assessment in the Mediterranean region under future climate scenarios, Earth Sci. Rev., 210 (2020) 103348. https://doi.org/10.1016/j.earscirev.2020.103348

[13] P. V. V Le, T. Phan-Van, K. V Mai, & D. Q. Tran, Space–time variability of drought over Vietnam, Int. J. Climatol., 39 (2019) 5437-5451. https://doi.org/10.1002/joc.6164

[14] I. Hatem, I. A. Alwan, A. R. T. Ziboon, and A. Kuriqi, Assessment of agricultural drought in Iraq employing Landsat and MODIS imagery, Open Engineering, 14 (2024) 20220583. https://doi.org/10.1515/eng-2022-0583

[15] Y. S. Almamalachy, A. M. F. Al-Quraishi, and H. Moradkhani. 2020. Agricultural drought monitoring over Iraq utilizing MODIS products, Environmental remote sensing and GIS in Iraq, pp. 253-278. Springer Cham. https://doi.org/10.1007/978-3-030-21344-2_11

[16] L. Said, N. Aziz, and L. Y. H. Al-Soudany, Spatiotemporal Mapping of Agricultural and Meteorological Drought in Wasit Province Based on GIS and Remote Sensing Data, Ecol. Eng. Environ. Technol., 25 (2024) 115-122. https://doi.org/10.12912/27197050/186869

[17] Z. T. Abdulrazzaq, R. H. Hasan, and N. A. Aziz, Integrated TRMM data and standardized precipitation index to monitor the meteorological drought, Civ. Eng. J., 5 (2019) 1590-1598.

[18] Touma, Danielle, Martinez, Carlos National Center for Atmospheric Research Staff (Eds). Last modified 2023-08-02 "The Climate Data Guide: CHIRPS: Climate Hazards InfraRed Precipitation with Station data (version 2).

[19] C. Funk, Pete Peterson, Martin Landsfeld, Diego Pedreros, James Verdin, et al., The climate hazards infrared precipitation with stations—a new environmental record for monitoring extremes, Sci. Data, 2 (2015) 150066. https://doi.org/10.1038/sdata.2015.66

[20] Zanaga, D., Van De Kerchove, R., Daems, D., De Keersmaecker, W., Brockmann, C., Kirches, G., Wevers, J., Cartus, O., Santoro, M., (2022). ESA WorldCover 10 m 2021 v200.

[21] K. Aryal, A. Apan, and T. Maraseni, Comparing global and local land cover maps for ecosystem management in the Himalayas, Remote Sens. Appl., 30 (2023) 100952. https://doi.org/10.1016/j.rsase.2023.100952

[22] T. Zhao, X. Zhang, Y. Gao, J. Mi, W. Liu, et al., Assessing the Accuracy and Consistency of Six Fine-Resolution Global Land Cover Products Using a Novel Stratified Random Sampling Validation Dataset, Remote. Sens. (Basel), 15 (2023) 2285. https://doi.org/10.3390/rs15092285

[23] M. Adnan Abdul Rahman, Characteristics of Rainfall in Dry and Wet Seasons in Iraq, Journal of the College of Education for Women, 33 (2022) 116-134. https://doi.org/10.36231/coedw.v33i1.1568

[24] M.-J. Fortin and M. Dale, Spatial analysis: a guide for ecologists. 2005. Accessed: Jun. 04, 2024. [Online]. Available: www.cambridge.org/9780521804349

[25] A. Liepa et al., Harmonized NDVI time-series from Landsat and Sentinel-2 reveal phenological patterns of diverse, small-scale cropping systems in East Africa, Remote Sens. Appl., 35 (2024) 101230. https://doi.org/10.1016/j.rsase.2024.101230

[26] K. S. Meshesha, E. Shifaw, A. Y. Kassaye, M. A. Tsehayu, A. A. Eshetu, and H. Wondemagegnehu, Evaluating the relationship of vegetation dynamics with rainfall and land surface temperature using geospatial techniques in South Wollo zone, Ethiopia, Environ. Challenges, 15 (2024) 100895. https://doi.org/10.1016/j.envc.2024.100895

[27] R. M. Fokeng and Z. N. Fogwe, Landsat NDVI-based vegetation degradation dynamics and its response to rainfall variability and anthropogenic stressors in Southern Bui Plateau, Cameroon, Geosyst. Geoenviron., 1 (2022) 100075. https://doi.org/10.1016/j.geogeo.2022.100075

[28] S. Paul et al., Assessment of endemic northern swamp deer (Rucervus duvaucelii duvaucelii) distribution and identification of priority conservation areas through modeling and field surveys across north India, Glob Ecol Conserv, 24 (2020) e01263. https://doi.org/10.1016/j.gecco.2020.e01263

[29] M. V Ferro, P. Catania, D. Miccichè, A. Pisciotta, M. Vallone, and S. Orlando, Assessment of vineyard vigour and yield spatio-temporal variability based on UAV high resolution multispectral images, Biosyst Eng., 231 (2023) 36-56. https://doi.org/10.1016/j.biosystemseng.2023.06.001

[30] H. A. Feizabadi, A. Mohammadi, G. Shahnaseri, and H. Y. Wan, Comparing drivers and protection of core habitat and connectivity for two sympatric desert carnivores, Glob. Ecol. Conserv., 48 (2023) e02696. https://doi.org/10.1016/j.gecco.2023.e02696

[31] X. Hua, R. Ohlemüller, and P. Sirguey, Differential effects of topography on the timing of the growing season in mountainous grassland ecosystems, Environ. Adv., 8 (2022) 100234. https://doi.org/10.1016/j.envadv.2022.100234

[32] S. Sannigrahi, Q. Zhang, P.K. Joshi, P. C. Sutton, S. Keesstra, et al., Examining effects of climate change and land use dynamic on biophysical and economic values of ecosystem services of a natural reserve region, J. Clean. Prod., 257 (2020) 120424. https://doi.org/10.1016/j.jclepro.2020.120424

[33] T. Zhang, C. Cheng, and S. Shen, Quantifying ecosystem quality in the Tibetan Plateau through a comprehensive assessment index, Environ. Sustainability Indic., 22 (2024) 100382. https://doi.org/10.1016/j.indic.2024.100382

[34] C. Wu and Z. Wang, Multi-scenario simulation and evaluation of the impacts of land use change on ecosystem service values in the Chishui River Basin of Guizhou Province, China, Ecol. Indic., 163 (2024) 112078. https://doi.org/10.1016/j.ecolind.2024.112078

[35] M. Luo, X. Jia, Y. Zhao, P. Zhang, and M. Zhao, Ecological vulnerability assessment and its driving force based on ecological zoning in the Loess Plateau, China, Ecol. Indic., 159 (2024) 111658. https://doi.org/10.1016/j.ecolind.2024.111658

[36] K. Yang , P. Zhou , J. Wu, Q. Yao, Z. Yang, Carbon stock inversion study of a carbon peaking pilot urban combining machine learning and Landsat images, Ecol. Indic., 159 (2024) 111657. https://doi.org/10.1016/j.ecolind.2024.111657

[37] B. Jasim, O. Jasim, and A. AL-Hameedawi, Monitoring Change Detection of Vegetation Vulnerability Using Hotspots Analysis, IIUM Eng. J., 25 (2024) 116–129. https://doi.org/10.31436/iiumej.v25i2.3030

[38] O. Aftergood and M. Flannigan, Identifying and analyzing spatial and temporal patterns of lightning-ignited wildfires in Western Canada from 1981 to 2018, Can. J. For. Res., 52 (2022). https://doi.org/10.1139/cjfr-2021-0353

[39] M. M. Yagoub and A. A. Al Yammahi, Spatial distribution of natural hazards and their proximity to heritage sites: Case of the United Arab Emirates, Int. J. Disaster Risk Reduct., 71 (2022) 102827. https://doi.org/10.1016/j.ijdrr.2022.102827

[40] R. Zhang, Y. Chen, X. Zhang, Q. Ma, and L. Ren, Mapping homogeneous regions for flash floods using machine learning: A case study in Jiangxi province, China, Int. J. Appl. Earth Obs. Geoinf., 108 (2022) 102717. https://doi.org/10.1016/j.jag.2022.102717

[41] J. Li, Z. Fang, J. Zhang, Q. Huang, and C. He, Mapping basin-scale supply-demand dynamics of flood regulation service – A case study in the Baiyangdian Lake Basin, China, Ecol. Indic., 139 (2022) 108902. https://doi.org/10.1016/j.ecolind.2022.108902

[42] Y. Zhang, J. Wua, S. Adilib, H. Zhangb, G. Shib, et al., Prevalence and spatial distribution characteristics of human echinococcosis: A county-level modeling study in southern Xinjiang, China, Heliyon, 10 (2024) e28812. https://doi.org/10.1016/j.heliyon.2024.e28812

[43] A. Ndagijimana, G. Nduwayezuc, C. Kagoyirec, A. Umubyeyib, A. Mansourianc et al., Childhood stunting is highly clustered in Northern Province of Rwanda: A spatial analysis of a population-based study, Heliyon, 10 (2022) e24922. https://doi.org/10.1016/j.heliyon.2024.e24922

[44] Z. Shi, D. Jiang, and Y. Wang, Spatiotemporal dependence of compound drought–heatwave and fire activity in China, Weather Clim Extrem, 45 (2024) 100695. https://doi.org/10.1016/j.wace.2024.100695

[45] B. Stumpe, B. Bechtel, J. Heil, C. Jörges, A. Jostmeier, et al., Soil texture mediates the surface cooling effect of urban and peri-urban green spaces during a drought period in the city area of Hamburg (Germany), Sci. Total Environ., 897 (2023) 165228. https://doi.org/10.1016/j.scitotenv.2023.165228

[46] A. Khoshnazar, G. Corzo, and M. Sajjad, Characterizing spatial–temporal drought risk heterogeneities: A hazard, vulnerability and resilience-based modeling, J. Hydrol, (2023) 129321. https://doi.org/10.1016/j.jhydrol.2023.129321

[47] K. Zhao, Michael A. Wulder, Tongxi Hu , Ryan Bright , Qiusheng Wu, et al., Detecting change-point, trend, and seasonality in satellite time series data to track abrupt changes and nonlinear dynamics: A Bayesian ensemble algorithm, Remote Sens. Environ., 232 (2019) 111181. https://doi.org/10.1016/j.rse.2019.04.034

[48] G. V. Laurin, A. Cotrina-Sanchez, L. Belelli-Marchesini, E. Tomelleri, G. Battipaglia, et al., Comparing ground below-canopy and satellite spectral data for an improved and integrated forest phenology monitoring system, Ecol. Indic., 158 (2024) 111328. https://doi.org/10.1016/j.ecolind.2023.111328

[49] Y. Ngadi Scarpetta, V. Lebourgeois, A.-E. Laques, M. Dieye, J. Bourgoin, and A. Bégué, BFASTm-L2, an unsupervised LULCC detection based on seasonal change detection – An application to large-scale land acquisitions in Senegal, Int. J. Appl. Earth Obs. Geoinf., 121 (2023) 103379. https://doi.org/10.1016/j.jag.2023.103379

[50] J. Mardian, A. Berg, and B. Daneshfar, Evaluating the temporal accuracy of grassland to cropland change detection using multitemporal image analysis, Remote Sens. Environ., 255 (2021) 112292. https://doi.org/10.1016/j.rse.2021.112292

[51] J. Li, Z.-L. Li, H. Wu, and N. You, Trend, seasonality, and abrupt change detection method for land surface temperature time-series analysis: Evaluation and improvement, Remote Sens. Environ., 280 (2022) 113222. https://doi.org/10.1016/j.rse.2022.113222

[52] F. Di Nunno, G. de Marinis, and F. Granata, Analysis of SPI index trend variations in the United Kingdom - A cluster-based and bayesian ensemble algorithms approach, J. Hydrol. Reg. Stud., 52 (2024) 101717. https://doi.org/10.1016/j.ejrh.2024.101717

[53] S. Mehri, A. A. Alesheikh, and A. Lotfata, Abiotic factors impact on oak forest decline in Lorestan Province, Western Iran, Sci. Rep., 14 (2024) 3973. https://doi.org/10.1038/s41598-024-54551-6

[54] A. Ganji, M. Saeedi, M. Lloyd, J. Xu, S. Weichenthal, and M. Hatzopoulou, Air pollution prediction and backcasting through a combination of mobile monitoring and historical on-road traffic emission inventories, Sci. Total Environ., 915 (2024) 170075. https://doi.org/10.1016/j.scitotenv.2024.170075

[55] E. Saghbiny, L. Leblanc, A. Harlé; C. Bobbio; R. Vialle, et al., Breach Detection in Spine Surgery Based on Cutting Torque, IEEE Trans. Med. Robot. Bionics., 1 (2024) 1084-1092. https://doi.org/10.1109/TMRB.2024.3421543

[56] R. Lyu, J. Pang, J. Zhang, and J. Zhang, The impacts of disturbances on mountain ecosystem services: Insights from BEAST and Bayesian network, Appl. Geogr., 162 (2024) 103143. https://doi.org/10.1016/j.apgeog.2023.103143

[57] M. Sakizadeh, A. Milewski, and M. T. Sattari, Analysis of Long-Term Trend of Stream Flow and Interaction Effect of Land Use and Land Cover on Water Yield by SWAT Model and Statistical Learning in Part of Urmia Lake Basin, Northwest of Iran, Water (Basel), 15 (2023) 690. https://doi.org/10.3390/w15040690

[58] Tongxi Hu, Yang Li, Xuesong Zhang, Kaiguang Zhao, Jack Dongarra, and Cleve Moler, Package 'Rbeast 1.23, 2023. https://pypi.org/project/Rbeast/

[59] S. Ali, Effect of irrigation water quality and nitrogen fertilizer in the growth of barley crop (hordeum vulgare l.) and some physical and chemical soil traits in dhi qar province, southern iraq, Plant Arch, 19 (2019) 2581-6063.

[60] A. Jabbar Khalaf Al meini, A Proposed Index of Water Quality Assessment for Irrigation, Eng. Technol. J., 28 (2010) 6557-6579. https://doi.org/10.30684/etj.28.22.9

[61] H. M. Hassan and H. S. Dakheel, Using the Normalized Difference Vegetation Index (NDVI) to study the change of vegetation cover in Thi-Qar Governorate, southern Iraq for the period from 1990-2022, Texas J. Agric. Biol. Sci., 13 (2023) 72-84.

[62] H. Kazim and A. Yassin, Detecting the state of drought and water deficit and its effects in Dhi Qar Governorate, Ibn Khaldun J. Stud. Res., 2 (2022) https://www.benkjournal.com/article/view/1080.

[63] N. Muhaisen, T. Khayyun, and M. Al-Mukhtar, Drought forecasting model for future climate change effects in a regional catchment area in northern Iraq, Eng. Technol. J., 42 (2024) 525–539. https://doi.org/10.30684/etj.2024.144458.1634

[64] R. Attafi, A. D. Boloorani, A. M Fadhil Al-Quraishi, and F. Amiraslani, Comparative analysis of NDVI and CHIRPS-based SPI to assess drought impacts on crop yield in Basrah Governorate, Iraq, Caspian J. Environ. Sci., 19 (2021) 547–557.